FEATURE

Designing a Low-Cost Spacecraft Simulator

Using a spacecraft simulator facility to educate undergrads in spacecraft attitude dynamics and control.

©DIGITAL STOCK

By ByungMoon Kim, Efstathios Velenis, Patrick Kriengsiri, and Panagiotis Tsiotras

Future commercial and military spacecraft are envisioned to have an unprecedented degree of autonomy and pointing accuracy, made possible by increased on-board processing speed and memory capabilities. These on-board capabilities are imperative for the demanding tasks of envisioned future space missions, such as very large base interferometry [1]-[3], deployment of space optical telescopes, formation flying [4]-[7], and autonomous spacecraft docking and servicing [8]-[11]. In the past several years, numerous spacecraft control techniques have been developed that address the challenging attitude tracking, stabilization, and disturbance rejection requirements for these missions.

One major aspect that has typically been missing in the area of satellite attitude control development is experimental validation of the available theoretical results. Experimental testing is essential before any novel control laws can be incorporated into future-generation spacecraft. The greatest difficulty in implementing spacecraft control laws is that ground-based experiments must take place in a 1-g environment, whereas the actual spacecraft will operate under 0-g conditions. Simulating a 0-g, torque-free environment is not an easy proposition. In fact, until recently, only a few government and industrial laboratories [12], [13] had the capability to experimentally validate attitude control laws in a realistic environment. With the recent expansion of the commercial as well as military satellite industries, there is an increased need for rapid prototyping and testing of the most promising attitude control algorithms proposed in the literature.

Several nongovernment agencies and academic institutions have recently initiated the development and construction of realistic simulators that can be used to educate the next generation of spacecraft dynamics and control engineers [14], [15]. This article describes the recent efforts at the Georgia Institute of Technology (GIT) to design, build, and test a relatively low-cost (approximately US$20,000) spacecraft simulator facility. The purpose of the GIT simulator is to evaluate and improve various controllers available in the literature and to develop new control strategies in an experimental framework. This simulator is also used to demonstrate the fun-

0272-1708/03/$17.00©2003IEEE

damentals of spacecraft attitude dynamics, attitude estimation, and control to undergraduate students at Georgia Tech.

In the sequel, the major components of the spacecraft simulator are described in detail. Accurate balancing of the platform is necessary to duplicate a torque-free environment. Perfect balancing is obtained when the center of gravity coincides with the center of rotation of the platform. To achieve this goal, an identification algorithm was developed to estimate the moment of inertia matrix and the center of gravity of the whole platform. This algorithm can also be used to estimate the inertia matrix for later use in attitude tracking and indirect adaptive control schemes. Results from the testing of a linear stabilizing controller are also reported at the end of the article.

Overview of the Spacecraft Platform

The "bus" of the GIT spacecraft simulator consists of a disk-shaped aluminum platform with a diameter of 60.96 cm (1.90 cm thick) that is supported on a hemispherical air bearing. The platform houses all the various spacecraft components (i.e., sensors, actuators, control computer; see Figure 1).

The air bearing is operated with compressed air from an external source through an air filter. The air filter removes moisture, oil, and other impurities and regulates the air pressure (roughly around 170-270 KPa depending on the normal load). Three wheels are mounted under the platform that can be operated in momentum or reaction wheel (RW) mode. The wheels are each paired with a dc motor and amplifier. Encoders that are installed on the dc motors provide angular position feedback. Power for the entire system is provided by six 12-V batteries connected pairwise in series to provide 24 V at a time.

On top of the platform, a PC104-type Pentium 266-MHz main computer board (CMP5e) is used for data acquisition, recording, controller implementation, and communication. The remote PC and the CMP5e communicate via wireless RF modems connected to their RS-232 serial ports. The remote

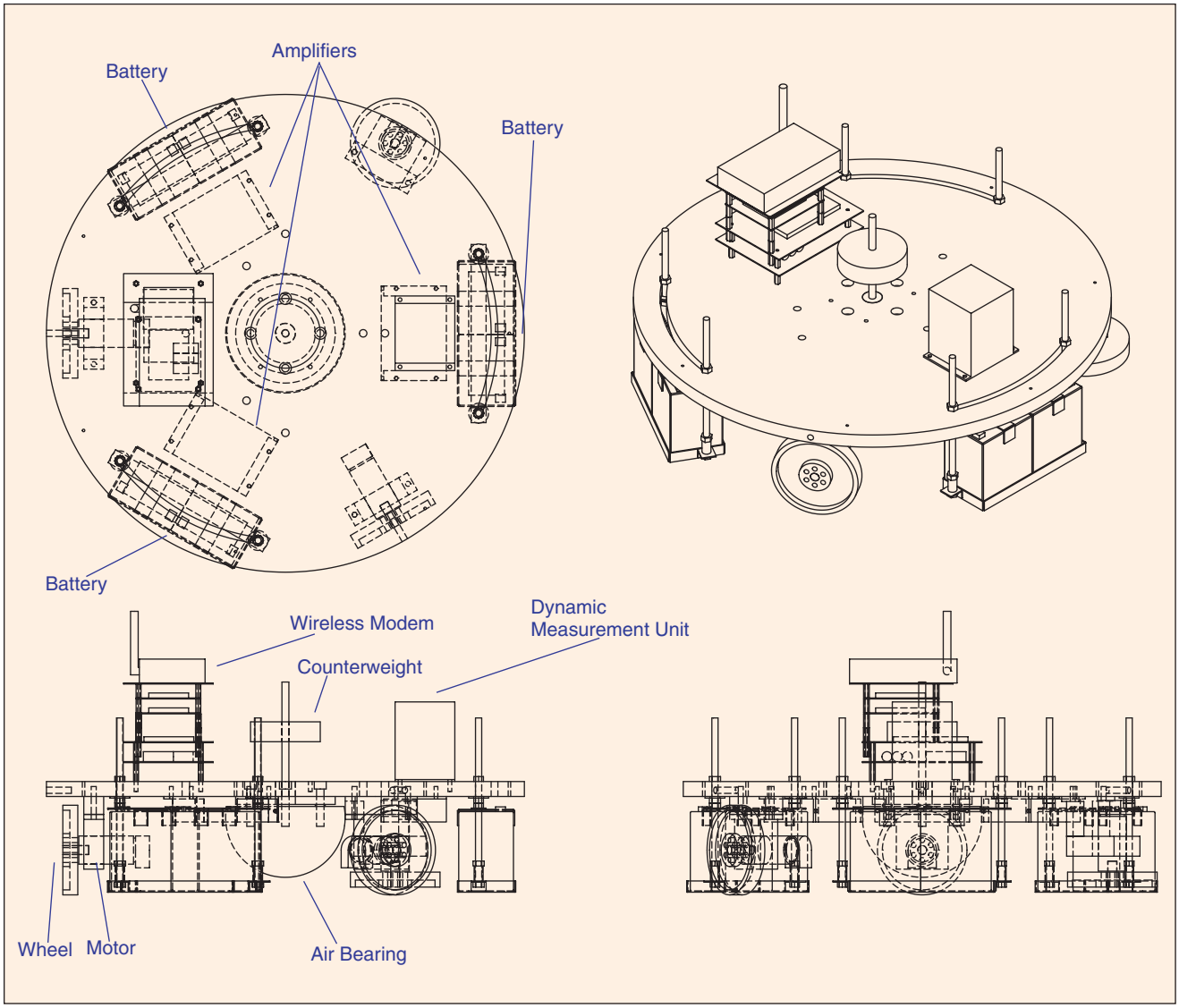

Figure 1. *Schematic of spacecraft platform and components.*

PC monitors the status of the experiments and issues control commands such as start/stop, whereas the CMP5e unit runs the control algorithm.

A photograph of the completed spacecraft simulator is shown in Figure 2. An outline of the interconnection of the several simulator subsystems is shown in Figure 3. In the next section, we briefly describe the major subsystems of the simulator.

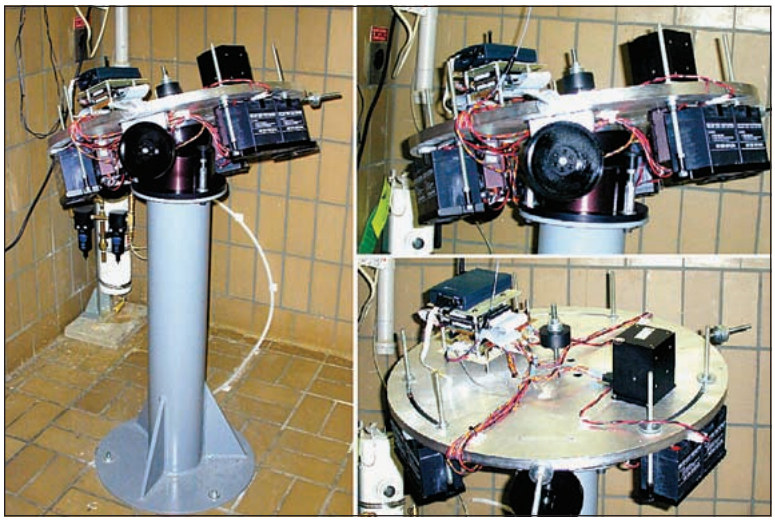

Figure 2. *The spacecraft simulator.*

Subsystem Description

Air Bearing, Platform, and Batteries

The air bearing that supports the platform is located on top of a pedestal structure (1 m high), and it allows the platform to move without friction ±30° about the two horizontal axes (x and y) and 360° about the vertical (z) axis. The bearing is the SRA 300 spherical air bearing designed and manufactured by Specialty Components Inc. The bearing itself is made of 6061 aluminum alloy hard-coated with Al_2O_3 and can hold up to 340 kg of load when operating at 550 Kpa air pressure. The GIT platform bearing is operated at 205 psi, which corresponds to approximately 135 kg of vertical load.

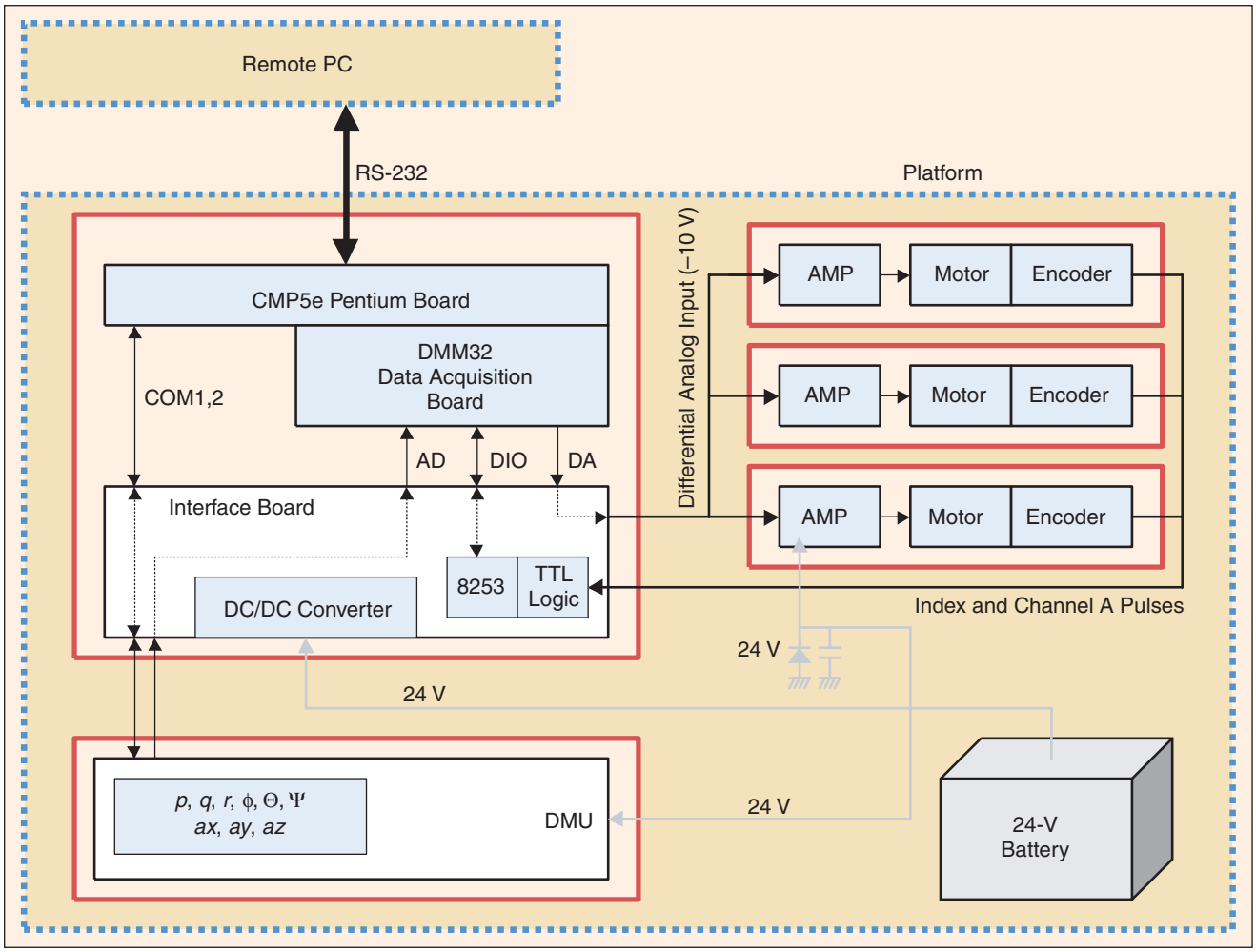

Figure 3. *Overview of the spacecraft simulator component interconnection.*

The platform on top of the air bearing provides a mounting surface for the simulator subsystems. The location of the center of mass (desired to be at the center of rotation of the simulator) can be changed by positioning several counterweights in various slots and holes located at several places on the platform. Care has been taken to position all major components of the simulator, such as momentum wheels, batteries, and amplifiers, in a symmetric fashion. This makes it easier to balance the platform, as well as to locate the principal axes.

Power to the simulator is provided by three pairs of rechargeable sealed lead acid batteries rated at 12 V and 5 Ah. Each pair of batteries is connected in series to provide 24 V. The batteries are then in turn connected to a dc/dc converter, which distributes the power to each spacecraft simulator component.

Spacecraft Attitude Sensor

The main purpose of the spacecraft simulator is to test several feedback attitude control laws. To implement the various controllers, measurements for the Eulerian angles and the angular rates are required. A dynamic measurement unit (DMU-AHRS) by Crossbow, Inc., was chosen as the attitude sensor unit. The DMU-AHRS provides the Eulerian angles, angular rates, and linear acceleration. It can measure roll and pitch angles of ±90° and heading angle of ±180°. The root mean square (RMS) noise level in Eulerian angle measurement signal is 0.1°. The angular rate range is ±150 °/s, and the RMS noise level is 0.05 °/s. The accelerometer range is ±2 g, and the RMS noise is 0.002 g. The accelerometer outputs were not used in our case. Note that the peak-to-peak noise is about six times higher than the RMS noise level. All the measured values are available in both RS-232 and analog signal output. The analog signal provides faster sampling rates, whereas the RS-232 port provides digital data directly without introducing additional noise. For convenience, the signals from the digital output were chosen after taking into account the requirements for noise-free operation.

Momentum Wheel Speed and Acceleration Sensor

Three encoders, rated at 500 counts/turn, are used to measure the angles of the momentum wheels. By differentiating the encoder outputs, the rotational velocities and accelerations of the wheels are calculated. A digital filter was designed to reduce the noise caused by the differentiation of the signal. Alternatively, a tachometer could have been used to measure angular velocity directly. Differentiation and filtering are still required to estimate angular acceleration in this case. We have used encoders instead of tachometers,

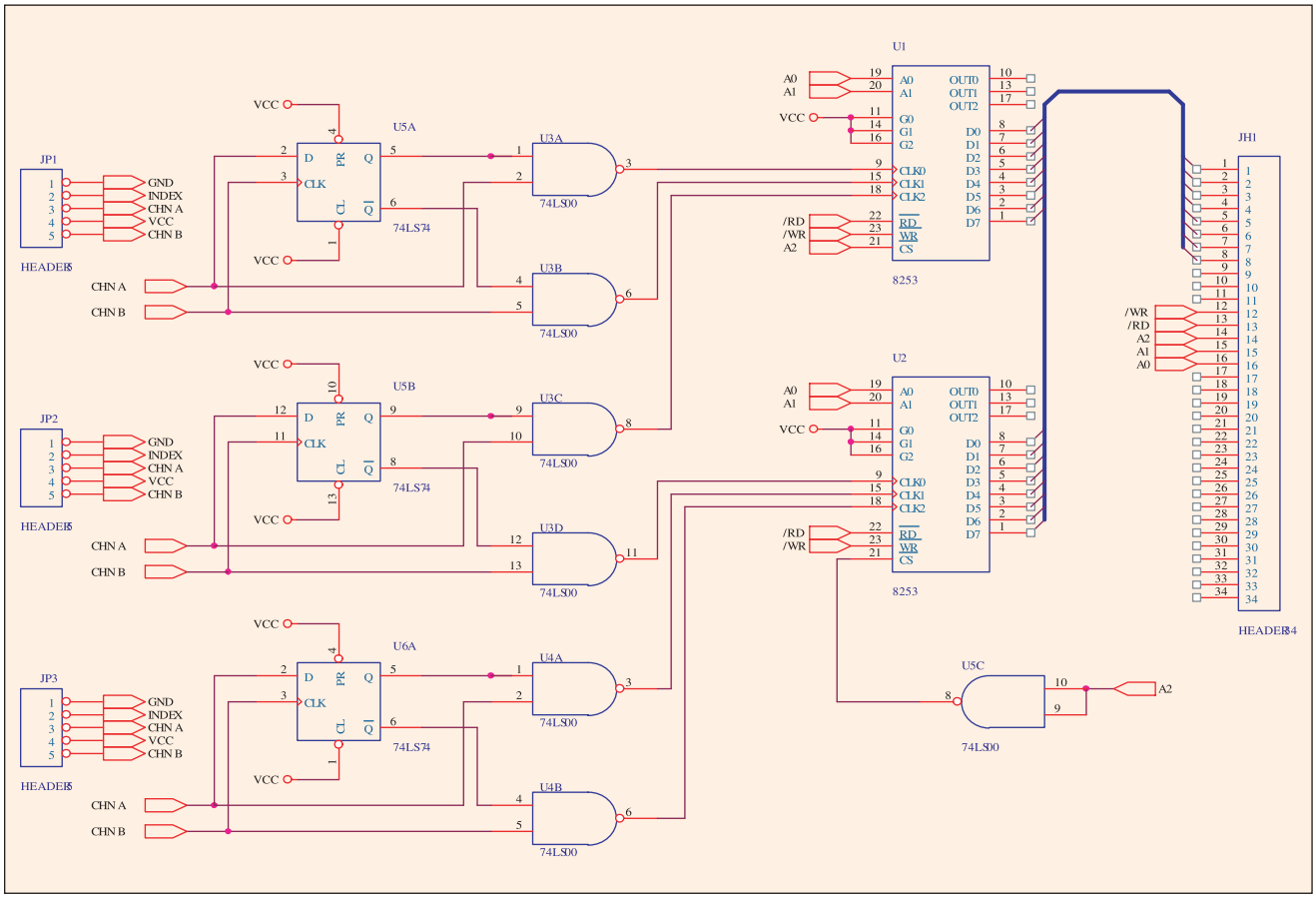

Figure 4. *Encoder signal processing: phase detection and wheel turn count.*

since the noise in the analog tachometer output can be avoided and small velocities can be measured more accurately with the encoder. One disadvantage of the encoders is that the time delay caused by filtering is typically larger than that for the tachometer. This delay, however, can be kept small by careful filter design.

A standard flip-flop circuit was used to decode the encoder signal [16]. Figure 4 shows the complete schematic of the encoder signal processing circuit. Note that two 8253 timers/counters are used. Each 8253 has three counters. Since the three encoders need six counters, all counters in both 8253s were used. The control signals for the 8253, i.e., address (A0,A1,A2), read (RD), write (WR), chip select (CS), and data signals (D0-D7), are connected to the digital interface of the I/O DMM32 board. The control signals A0, A1, A2, RD, WR, and CS were implemented in software.

Wheels, Motors, and Power Amplifiers

Three Maxon dc motors (Model 143683) with a 24-V nominal voltage were used as actuators in lieu of expensive, space-certified reaction/momentum wheels. The three wheels are made of steel. The stall torque of each dc motor is 783 mNm, the maximum continuous torque is 88.8 mNm, and the maximum permissible speed is 8200 rpm. Each motor is driven by a power amplifier made by Copley Control (Model 403). It can deliver continuous power of 120 W (24-V input) and peak power of 240 W (24 V input). The amplifier generates a PWM output for precise torque control. During initial testing, this power amplifier was observed to produce negative voltage in a counterclockwise spin, which can damage the power supply circuit or other electronic components. Therefore, a diode (D1 in Figure 5) was used to clip the negative voltage caused by the amplifier, and a capacitor (C1 in Figure 5) was used to flatten the power fluctuation. The power distribution schematic is shown in Figure 5.

The CPU, I/O, and Interface Boards

The electronics suite includes the CPU unit, the I/O board, interface board, and RF modem. The CPU board runs the software that handles all hardware controls, timers, packet-based communication, and the filters for the sensor signals. A PC104-type Intel mobile Pentium 266-MHz board (model CMP5e from Ampro Computers) was used as the CPU. It has 32 MB of main memory, an 8-MB memory disk, and two serial ports. To meet all I/O requirements, a PC104-type analog interface board (DMM32 from Diamond Systems Corp.) was installed on top of the CMP5e. This board has 32 single-ended or 16 differential, 16-bit A/D converters with a sampling rate of 200 kHz, four 12-bit D/A converters, and 24 programmable digital I/O. An interface board provides terminals for power and communication, as well as sensor signals for easy interface. Placed on the interface board is also a dc/dc converter for 5-, 12-, and 15-V voltage sources for various components. Another option is to use a regulator to provide the necessary voltage levels to the various spacecraft components. This board also has flip-flops and counters to measure the encoder signals (see the previous section). These counters are interfaced to the DMM32 via the digital I/O ports of the DMM32. The interface board was designed and built in-house.

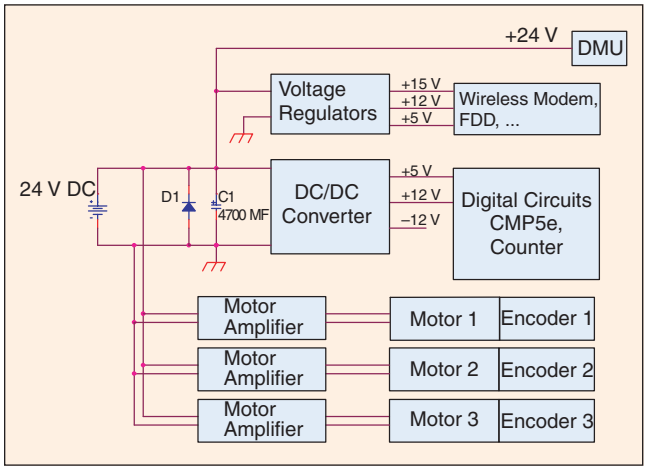

Figure 5. *Power distribution diagram.*

Software

Two software applications were developed separately for both the CMP5e on-board computer and the remote PC computer. The latter is used to send start/stop commands and commands for health monitoring, for postexperiment data analysis and plotting. The CMP5e and the remote host computers communicate via a wireless RF serial modem at a speed of 56 K baud. The executable module for the CMP5e implements hardware initialization and controller initialization; it also starts a 0.1-ms precision timer to schedule various tasks and communication. The user can set up the main control loop frequency. A frequency of 100 Hz was used for all experiments described in this article.

The remote PC runs a separate view-based graphical user interface (GUI) program that implements the control toolbar, monitor view, message view, and other GUIs. The programs on the remote PC and the on-board computer communicate through the wireless RS-232 serial connection with four types of custom-developed packets: data, message, file, and command packets. During the experiment, the time histories of all state variables are recorded in the memory disk of the CMP5e in binary format. After the experiment, the data file is transferred to the host PC, where it is converted to a MATLAB *.mat file for further analysis.

Filtering and Identification of Motor Parameters

Filter Design

Since the encoder signal from the motor only provides angular information, we need to differentiate it once to get angular rate and then once more to obtain angular acceleration, if necessary. Since differentiation of sensor signals always amplifies noise, filtering of the signal is necessary. A Butterworth or a Chebyshev type 1 filter can

be used for this purpose, depending on the high-frequency attenuation and time delay limitations. The frequency responses for both filters are shown in Figure 6. For all experiments described in this article, a Butterworth filter was chosen because of its smaller delay. Note that a sampling frequency of 100 Hz was used for all experiments. It is assumed that the spacecraft is moving slowly, and thus the delay of 0.1 s caused by the filter can be ignored; if necessary, this delay can be taken into account with more sophisticated control design methods.

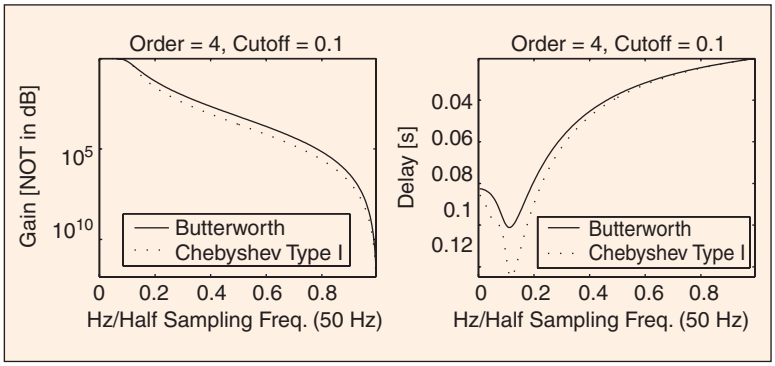

Figure 6. *Filter design.*

Estimation of Motor Damping and Choice of Reaction Wheels

To keep the output torque sufficiently larger than the friction torque, it is important to know the friction effects of the motor. This allows proper sizing of the momentum wheels. To estimate the damping torque of the motor, the wheel was spun up to a high speed and then the motor/wheel was left to decelerate. Since the inertia of the wheel is accurately known, one can estimate the magnitude of the damping torque. Figure 7 is the result of this experiment when the motor axis is horizontal; it shows viscous friction and dry friction (stiction). These damping torques can be an important factor affecting the sizing of the wheels. Larger wheels provide a larger torque and smaller damping. Smaller wheels provide good resolution in torque output, but they also have more damping since they usually operate at higher speeds.

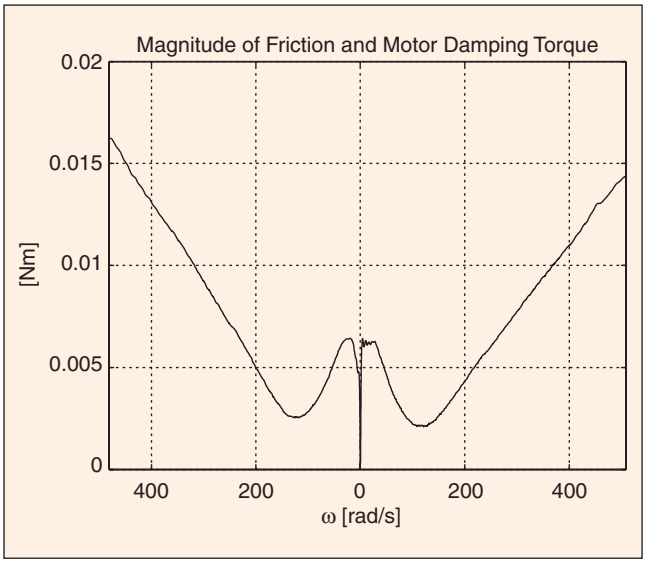

Figure 7. *Absolute value of friction torque versus speed during deceleration.*

Identification of Motor Dynamics

The static motor gain can be calculated from the specifications of the motor, the D/A converter setting, and the motor amplifier gain. A least-squares fit was used for identification of the motor transfer function. Figure 8 shows the transfer function from voltage input to the amplifier to torque output. The gain of the motor is about 0.48 Nm/V at zero frequency and decreases at higher frequency. As shown in this figure, the motor bandwidth is quite high, and the gain does not change much up to approximately 10 rad/s. This frequency is high enough compared to spacecraft rigid-body response (typically about 1 rad/s). Thus, it was decided that no additional effort to improve the motor response was required.

Identification of Moment of Inertia Matrix

One way of calculating the moments of inertia (MOI) of the rigid spacecraft simulator is to use a CAD model. An AutoCAD model for the whole assembly was thus developed, and mass densities for the various components were assigned for the entire system (see Figure 1). This model was detailed enough to include small components such as bolts and nuts. The mass distribution of the sensor and all other electrical components was assumed to be homogeneous; the electrical wires and some other small electrical parts were neglected. This method gives a fairly accurate estimate of the inertia

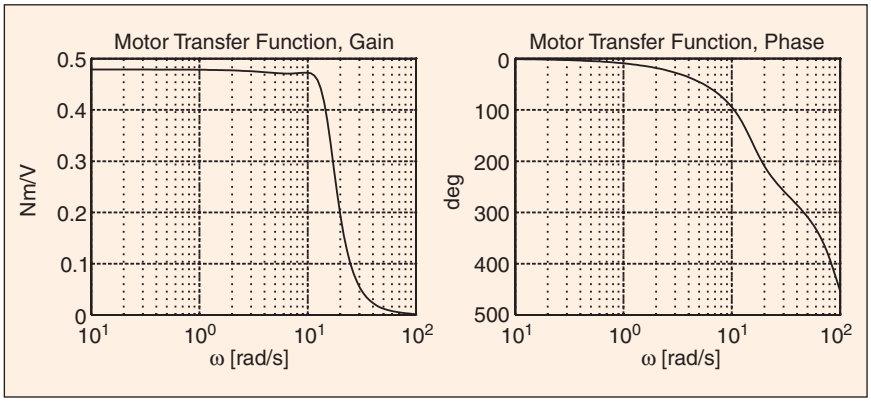

Figure 8. *Identified motor dynamics.*

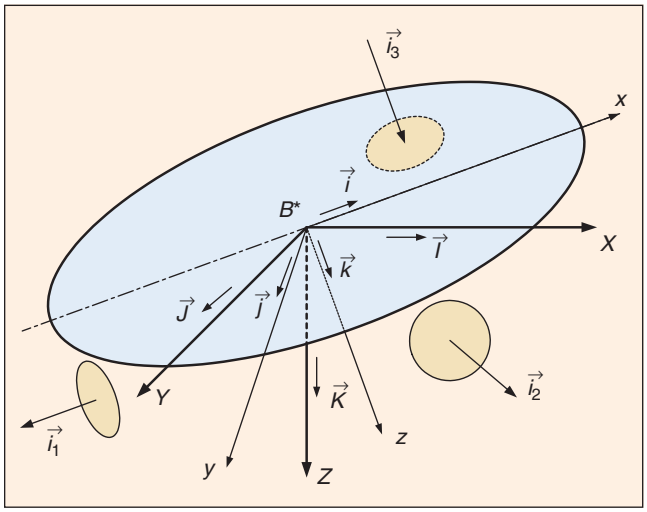

Figure 9. *Definition of coordinates.*

matrix. One drawback of generating the MOI estimation matrix using a technical drawing package such as AutoCAD is the difficulty associated with designing a complex 3-D CAD model. Alternatively, experimental methods can be used that are not affected by the complexity of the structure. Traditional pendulum methods, for instance, can be used to determine the inertia values from the period of the pendulum.

Other experimental methods, such as those described in [17] and [18], measure the external reaction forces induced by load cells and find the inertia matrix that best fits the equation of motion in a least-squares sense. The major drawback of such methods is the significant amount of effort required for setting up and conducting the experiments. Luckily, no such load cells are necessary for the spacecraft simulator. The spacecraft simulator operates in a torque-free (or almost torque-free) environment, and, in addition, it has fully featured motion sensors, which makes the experimental inertia estimation much simpler. Torque-free methods also have been proposed in the literature for inertia estimation. For example, in [19], the authors used a coasting maneuver. A solution was found after converting the full nonlinear equation of motion to a standard least-squares form. An optimal coasting maneuver was also proposed based on stochastic analysis of the sensor noise. An MOI estimation algorithm based on conservation of the angular momentum is also given in [20]. When the inertia of the spacecraft is changing, another approach is to use real-time inertia estimation strategies. Bergmann et al. [21] proposed a mass property estimation strategy using nonlinear filtering, together with a simplified (nonlinear) model for the equations of motion. An input selection method to generate a feasible inertia estimation maneuver for this estimator has been proposed in [22]. Other approaches for inertia estimation are those often found in the spacecraft adaptive control literature [23], [24].

Below we describe the moment of inertia and center of gravity estimation scheme used for the GIT spacecraft simulator. The method is based on a standard least-squares identification algorithm using a series of experiments. In each experiment, a torque profile is commanded and the angular accelerations of the platform are recorded. Offline analysis of the input-output data gives a very accurate estimation of both the moment of inertia matrix and the center of gravity of the platform. For comparison, the numerical values of the MOI and the center of mass obtained from an AutoCAD model are also provided.

Representation of Attitude Kinematics

A schematic of the spacecraft platform is shown in Figure 9. Let $\mathcal{I}$ denote the inertial frame and $\mathcal{S}$ denote a body-fixed frame, both with their origin at the geometric center of the bearing, denoted by B^* in Figure 9. Let $\{\vec{I},\vec{J},\vec{K}\}$ and $\{\vec{i},\vec{j},\vec{k}\}$ denote the basis unit vectors of the frames $\mathcal{I}$ and $\mathcal{S}$, respectively. Finally, let the unit vectors along the three wheel axes be denoted by $\{\vec{i}_1,\vec{i}_2,\vec{i}_3\}$.

The unit vectors $\vec{i}_{1,2,3}$ are given in the body frame as follows:

$$\vec{i}_1 = -\vec{i}, \quad \vec{i}_2 = \frac{1}{2}\vec{i} + \frac{\sqrt{3}}{2}\vec{j}, \quad \vec{i}_3 = \vec{k}.$$

To describe the attitude of the spacecraft, a 3-2-1 Eulerian angle sequence is used [25]. The direction cosine matrix (DCM), which represents the transformation from the inertial to the spacecraft body frame, is given by the equation shown at the bottom of the page. The kinematic equations for a 3-2-1 Eulerian angle sequence are given by [25]

$$\begin{Bmatrix}\dot{\phi}\\ \dot{\theta}\\ \dot{\psi}\end{Bmatrix} = \begin{bmatrix}1 & \sin\varphi\tan\theta & \cos\phi\tan\theta\\ 0 & \cos\phi & -\sin\phi\\ 0 & \sin\phi/\cos\theta & \cos\phi/\cos\theta\end{bmatrix}\begin{Bmatrix}p\\ q\\ r\end{Bmatrix}, \tag{1}$$

where p,q, and r are the components of the body angular velocity vector along the body $\vec{i}$, $\vec{j}$, and $\vec{k}$ axes, respectively.

Equations of Motion

The full nonlinear equations of motion can be derived starting from the momentum of a differential mass element dm as illustrated in Figure 10. Note that the center of mass of the platform is located at S^*. Let the angular velocity of the platform with respect to the inertial frame be denoted by ${}^I\vec{\omega}^S$, and let the angular velocity of the ℓth wheel with respect to the platform be denoted by ${}^S\vec{\omega}^{W_\ell}$.

The velocity of dm is given by $\vec{v} = {}^I\vec{\omega}^S \times \vec{r}$, where $\vec{r}$ is the position vector from the bearing center B^*.

$$R_S^I = \begin{bmatrix}\cos\theta\cos\psi & \cos\theta\ \sin\psi & -\sin\theta\\ \sin\phi\sin\theta\cos\psi - \cos\phi\sin\psi & \sin\phi\ \sin\theta\ \sin\psi + \cos\phi\ \cos\psi & \sin\phi\cos\theta\\ \cos\varphi\ \sin\theta\ \cos\psi + \sin\phi\ \sin\psi & \cos\phi\sin\theta\sin\psi - \sin\phi\cos\psi & \cos\phi\cos\theta\end{bmatrix}.$$

Similarly, the velocity of a differential mass dm of the wheel is given by

$$\vec{v}_{w_\ell} = {}^I\vec{\omega}^S \times \vec{r}_{w_\ell} + {}^S\vec{\omega}^{W_\ell} \times \vec{\rho}, \quad \ell = 1,2,3.$$

The angular momentum of the whole system with respect to B^* is then calculated as

$$\begin{aligned}
\vec{H} &= \int_S \vec{r} \times \left({}^I\vec{\omega}^S \times \vec{r}\right) \mathrm{d}m + \sum_{\ell=1}^{3} \int_{W_\ell} \vec{r}_{w_\ell} \times \left({}^I\vec{\omega}^S \times \vec{r}_{w_\ell} + {}^S\vec{\omega}^{W_\ell} \times \vec{\rho}\right) \mathrm{d}m \\
&= \int_{S+W} \vec{r} \times \left({}^I\vec{\omega}^S \times \vec{r}\right) \mathrm{d}m + \sum_{\ell=1}^{3} \int_{W_\ell} \vec{r}_{W_\ell} \times \left({}^S\vec{\omega}^{W_\ell} \times \vec{\rho}\right) \mathrm{d}m \\
&= \underline{\underline{\mathbf{I}}}^{(S+W)/B^*} \cdot {}^I\vec{\omega}^S + \sum_{\ell=1}^{3} \vec{r}_{w_\ell^*} \times \left({}^S\vec{\omega}^{W_\ell} \times \int_{W_\ell} \vec{\rho}\, \mathrm{d}m\right) + \sum_{\ell=1}^{3} \int_{W_\ell} \vec{\rho} \\
&\quad \times \left({}^S\vec{\omega}^{W_\ell} \times \vec{\rho}\right) \mathrm{d}m \\
&= \underline{\underline{\mathbf{I}}}^{(S+W)/B^*} \cdot {}^I\vec{\omega}^S + \sum_{\ell=1}^{3} \underline{\underline{\mathbf{I}}}^{W_\ell/W_\ell^*} \cdot {}^S\vec{\omega}^{W_\ell},
\end{aligned}$$

where $\underline{\underline{\mathbf{I}}}^{W_\ell/W_\ell^*}$ is the inertia dyadic of the ℓth wheel with respect to the wheel's mass center W_ℓ^* and $\underline{\underline{\mathbf{I}}}^{(S+W)/B^*}$ is the inertia dyadic for the entire body of spacecraft and wheels with respect to bearing center B^*. For convenience, let $\underline{\underline{\mathbf{I}}} \equiv \underline{\underline{\mathbf{I}}}^{(S+W)/B^*}$ and $\underline{\underline{\mathbf{I}}}^{\ell} \equiv \underline{\underline{\mathbf{I}}}^{W_\ell/W_\ell^*}$. Since viscosity effects of the air bearing are neglected and pressure is always normal to the spherical bearing surface, the only external torque exerted on the bearing center is caused by gravity. Euler's theorem gives the equations of motion of the platform as

$$\begin{aligned}
\vec{G} &= \vec{r}_S \times mg\vec{K} = \left(mg\ \vec{r}_S\right) \times \vec{K} \\
&= {}^S\frac{\mathrm{d}}{\mathrm{d}t}\left(\underline{\underline{\mathbf{I}}} \cdot {}^I\vec{\omega}^S\right) + {}^I\vec{\omega}^S \times \underline{\underline{\mathbf{I}}} \cdot {}^I\vec{\omega}^S \\
&\quad + \sum_{\ell=1}^{3} \left({}^{w_\ell}\frac{\mathrm{d}}{\mathrm{d}t}\left(\underline{\underline{\mathbf{I}}}^{\ell} \cdot {}^S\vec{\omega}^{W_\ell}\right) + {}^I\vec{\omega}^{W_\ell} \times \underline{\underline{\mathbf{I}}}^{\ell} \cdot {}^S\vec{\omega}^{W_\ell} \right) \\
&= \underline{\underline{\mathbf{I}}} \cdot {}^I\dot{\vec{\omega}}^S + {}^I\vec{\omega}^S \times \underline{\underline{\mathbf{I}}} \cdot {}^I\vec{\omega}^S \\
&\quad + \sum_{\ell=1}^{3} \left(\underline{\underline{\mathbf{I}}}^{\ell} \cdot {}^S\dot{\vec{\omega}}^{W_\ell} + \left({}^I\vec{\omega}^S + {}^S\vec{\omega}^{W_\ell}\right) \times \underline{\underline{\mathbf{I}}}^{\ell} \cdot {}^S\vec{\omega}^{W_\ell} \right).
\end{aligned}$$

Let the unit vector along the symmetry axis of the wheel W_ℓ ($\ell = 1,2,3$) be denoted by $\vec{i}_\ell$ and choose the other two bases vectors $\vec{j}_\ell$ and $\vec{k}_\ell$ so that they are orthonormal and form a right-handed coordinate system. Since the wheels are axisymmetric, $\underline{\underline{\mathbf{I}}}^{\ell} = I_{11}^{w_\ell}\vec{i}_\ell\vec{i}_\ell + I_{22}^{w_\ell}\vec{j}_\ell\vec{j}_\ell + I_{33}^{w_\ell}\vec{k}_\ell\vec{k}_\ell$. Also, since the wheels always rotate about $\vec{i}_\ell$, ${}^S\vec{\omega}^{W_\ell} = \omega_\ell\vec{i}_\ell$. As a result,

$$\begin{aligned}
{}^S\vec{\omega}^{W_\ell} \times \underline{\underline{\mathbf{I}}}^{\ell}\ {}^S\vec{\omega}^{W_\ell} &= \omega_\ell\vec{i}_\ell \times \left(I_{11}^{w_\ell}\vec{i}_\ell\vec{i}_\ell + I_{22}^{w_\ell}\vec{j}_\ell\vec{j}_\ell + I_{33}^{w_\ell}\vec{k}_\ell\vec{k}_\ell\right) \cdot \omega_\ell\vec{i}_\ell \\
&= \omega_\ell\vec{i}_\ell \times \left(I_{11}^{w_\ell}\omega_\ell\vec{i}_\ell\right) = 0, \qquad \ell = 1,2,3.
\end{aligned}$$

Finally, we have

$$\left(mg\ \vec{r}_S\right) \times \vec{K} = \underline{\underline{\mathbf{I}}} \cdot {}^I\dot{\vec{\omega}}^S + {}^I\vec{\omega}^S \times \underline{\underline{\mathbf{I}}} \cdot {}^I\vec{\omega}^S + \sum_{\ell=1}^{3} \left(\underline{\underline{\mathbf{I}}}^{\ell} \cdot {}^S\dot{\vec{\omega}}^{W_\ell} + {}^I\vec{\omega}^S \times \underline{\underline{\mathbf{I}}}^{\ell} \cdot {}^S\vec{\omega}^{W_\ell} \right). \tag{2}$$

Estimation of the Inertia Matrix

Since our experimental platform uses three momentum wheels, we can achieve arbitrary motion by sending acceleration commands to the wheels. The only external torque is caused by gravity; the center of gravity can be identified along with the inertia matrix. The estimation scheme uses the fact that the equations of motion (2) are linear with respect to the inertia parameters and the gravity term. Thus, the estimation problem can be solved easily by a least-squares algorithm implemented in regression form [19], as described below. During identification, wheel acceleration commands are applied along all three body axes. Since the platform cannot exceed pitch and roll in excess of ±30°, a stabilizing LQR controller is turned on to reorient the platform to the initial position if the angular pitch and roll motions exceed these values.

We now rewrite (2) in matrix form. To this end, let $R_S^{W_\ell}$ be the transformation matrix from the frame of the ℓth wheel $\{\vec{i}_\ell, \vec{j}_\ell, \vec{k}_\ell\}$ to frame $\mathcal{S}$. From Figure 11, the matrices $R_S^{W_\ell}$, $\ell = 1,2,3$ are given as

$$R_S^{W_1} = \begin{bmatrix} -1 & 0 & 0 \\ 0 & -1 & 0 \\ 0 & 0 & 1 \end{bmatrix}, \quad R_S^{W_2} = \begin{bmatrix} 1/2 & -\sqrt{3}/2 & 0 \\ \sqrt{3}/2 & 1/2 & 0 \\ 0 & 0 & 1 \end{bmatrix},$$

$$R_S^{W_3} = \begin{bmatrix} 0 & 0 & -1 \\ 0 & 1 & 0 \\ 1 & 0 & 0 \end{bmatrix}.$$

Let $\{\vec{\omega}\}_S$ and $[\underline{\underline{\mathbf{I}}}]_S$ denote the vector $\vec{\omega}$ and the dyadic $\underline{\underline{\mathbf{I}}}$ expressed in the frame $\mathcal{S}$. Also, let $[\tilde{\omega}]_S$ denote the cross-

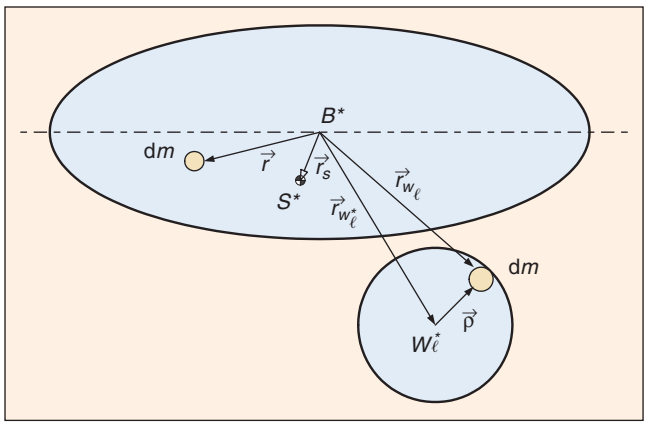

Figure 10. *Definition of mass center and momentum of an elementary mass* dm.

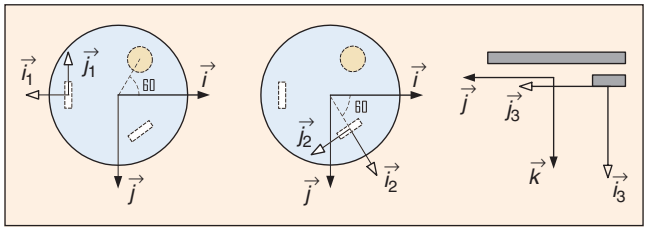

Figure 11. *Coordinate transformations.*

product operator of the vector $\{\vec{\omega}\}_S$ in matrix form [25]. Using the fact that $\underline{\underline{\mathbf{I}}}^{\ell} \cdot {}^{S}\vec{\omega}^{W_\ell} = I_{11}^{w_\ell}\omega_\ell \vec{i}_\ell$ and letting $\{{}^I\vec{\omega}^S\}_S \equiv [p \;\; q \;\; r]^T$, one obtains

$$\left\{\vec{G}\right\}_S := mg\left\{\vec{r}_S \times \vec{K}\right\}_S = -\left[\tilde{K}\right]_S \left\{mg\;\; \vec{r}_S\right\}_S,$$

where $\{\vec{G}\}_S$ is the gravity torque vector expressed in the $\mathcal{S}$ frame and $\{\vec{K}\}_S$ is

$$\left\{\vec{K}\right\}_S = \begin{Bmatrix} \vec{i}\cdot\vec{K} \\ \vec{j}\cdot\vec{K} \\ \vec{k}\cdot\vec{K} \end{Bmatrix} = \begin{Bmatrix} -\sin\theta \\ \sin\phi\cos\theta \\ \cos\phi\cos\theta \end{Bmatrix}.$$

Equation (2) can now be written as

$$\begin{aligned} 0 &= \left[\tilde{K}\right]_S \left\{mg\;\; \vec{r}_S\right\}_S + \left[\underline{\underline{\mathbf{I}}}\right]_S \left\{{}^I\dot{\vec{\omega}}^S\right\}_S + \left[{}^I\tilde{\omega}^S\right]_S \left[\underline{\underline{\mathbf{I}}}\right]_S \left\{{}^I\vec{\omega}^S\right\}_S \\ &\quad + \sum_{\ell=1}^{3} \left(R_S^{W_\ell} \begin{Bmatrix} I_{11}^{w_\ell}\dot{\omega}_\ell \\ 0 \\ 0 \end{Bmatrix} + \left[{}^I\tilde{\omega}^S\right]_S R_S^{W_\ell} \begin{Bmatrix} I_{11}^{w_\ell}\omega_\ell \\ 0 \\ 0 \end{Bmatrix} \right) \\ &:= Ax - T, \end{aligned}$$

where $A \in \mathbb{R}^{3\times 9}$, $x \in \mathbb{R}^{9\times 1}$, and $T \in \mathbb{R}^{3\times 1}$ are given by

$$A = \left[\begin{array}{cccccc|c} \dot{p} & \dot{q}-pr & \dot{r}+pq & -qr & q^2-r^2 & qr & \\ pr & \dot{d}+qr & r^2-p^2 & \dot{q} & \dot{r}-pq & -pr & \left[\tilde{K}\right]_S \\ -pq & p^2-q^2 & \dot{p}-qr & pq & \dot{q}+pr & \dot{r} & \end{array}\right]$$

$$x = \left[I_{11} \;\; I_{12} \;\; I_{13} \;\; I_{22} \;\; I_{23} \;\; I_{33} \;\; mg\, r_{S_x} \;\; mg\, r_{S_y} \;\; mg\, r_{S_z}\right]^T$$

$$T = -\begin{Bmatrix} -I_{11}^{w_1}\dot{\omega}_1 + \frac{1}{2}I_{11}^{w_2}\dot{\omega}_2 \\ \frac{\sqrt{3}}{2}I_{11}^{w_2}\dot{\omega}_2 \\ I_{11}^{w_3}\dot{\omega}_3 \end{Bmatrix} - \begin{bmatrix} 0 & -r & q \\ r & 0 & -p \\ -q & p & 0 \end{bmatrix} \begin{Bmatrix} -I_{11}^{w_1}\omega_1 + \frac{1}{2}I_{11}^{w_2}\omega_2 \\ \frac{\sqrt{3}}{2}I_{11}^{w_2}\omega_2 \\ I_{11}^{w_3}\omega_3 \end{Bmatrix}.$$

Let A_k and T_k denote the values of A and T at the kth time step, and define $\overline{A}_k$ and $\overline{T}_k$ as

$$\overline{A}_k = \begin{bmatrix} A_1 \\ A_2 \\ \vdots \\ A_k \end{bmatrix} \in \mathbb{R}^{3k\times 9}, \quad \overline{T}_k = \begin{Bmatrix} T_1 \\ T_2 \\ \vdots \\ T_k \end{Bmatrix} \in \mathbb{R}^{3k\times 1}.$$

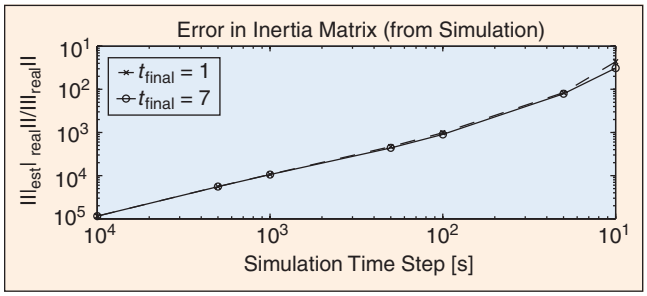

Figure 12. *Verification of estimation equations by simulation.*

Finally, the least-squares estimation of x at time step $t = t_k$ (denoted by $\hat{x}_k$) that minimizes $\left\|\overline{A}_k x - \overline{T}_k\right\|$ is given by

$$\hat{x}_k = \overline{A}_k^{\dagger}\overline{T}_k, \tag{3}$$

where $\overline{A}_k^{\dagger}$ is the pseudo-inverse of $\overline{A}_k$. Assuming that $\overline{A}_k$ is full-column rank, then its pseudo-inverse can be calculated as $\overline{A}_k^{\dagger} = (\overline{A}_k^T\overline{A}_k)^{-1}\overline{A}_k^T$.

To verify the regression equation $\overline{A}_k x = \overline{T}_k$ and investigate the effect of numerical errors incurred during the matrix pseudo-inversion (3), the previous inertia estimation scheme was tested using simulated data. A simple angular velocity stabilizing control law was used for the simulation. The results are shown in Figure 12. Note that the error decreases as the simulation time step decreases. Thus, we may conclude that the numerical error during the matrix inversion in (3) is negligible.

The least-squares estimation algorithm described above is straightforward but requires many data points to be processed in a batch mode so as to ensure good results. In addition, this approach is not very efficient since, with every new sample, the whole regressor matrix has to be inverted from scratch. Alternatively, a *recursive* least-squares estimation approach can be used to avoid the direct calculation of the pseudo-inverse in (3).

The main idea behind recursive least-squares estimation [26] is that the estimated value of x at the kth time step, $\hat{x}_k$, can be obtained from its estimated value at the $(k-1)$th time step. To this end, let P_k^{-1} denote the matrix

$$P_k^{-1} := \overline{A}_k^T\overline{A}_k = \sum_{i=1}^{k} A_i^T A_i,$$

which implies that at each time step, the matrix P_k can be updated from the kth regressor matrices. Given P_0 and $\hat{x}_0$, the least-squares estimate $\hat{x}_k$ satisfies the following recursive equations:

$$\begin{aligned} \hat{x}_k &= \hat{x}_{k-1} + L_k\left(T_k - A_k\hat{x}_{k-1}\right) \\ L_k &= P_kA_k = P_{k-1}A_k^T\left(I + A_kP_{k-1}A_k^T\right)^{-1} \\ P_k &= (I - K_kA_k)P_{k-1}. \end{aligned}$$

The estimate $\hat{x}_k$ is obtained by adding a correction to the estimate at the previous time step, $\hat{x}_{k-1}$. The correction term is proportional to the difference between the measured value T_k at the kth time step and the prediction of the observation based on the previous parameter estimate, given by $A_k\hat{x}_{k-1}$. The components of the vector L_k are weighting factors that tell us how the correction and the previous estimate should be combined. Notice that the matrix P_k is defined only when the matrix $\overline{A}_k^T\overline{A}_k$ is nonsingular. To avoid singularities, the recursive equations are initialized with a sufficiently large positive definite matrix P_0.

Experimental Results

The previous algorithm assumes knowledge of the moments of inertia of the wheels. These were calculated from AutoCAD.

Since the geometric complexity of the wheels is simple, it is assumed that the inertia values of the wheels from the CAD model were accurate. These values are given below:

$$I_{11}^{w_1} = I_{11}^{w_2} = I_{11}^{w_3} = 1.792 \times 10^{-3} \quad (\text{kg m}^2).$$

The following results show the averaged values for the inertia matrix and the vector $mg\vec{r}_s$ from a series of ten experiments. Each experiment was performed for about 50-80 s. For comparison, the inertia matrix calculated from AutoCAD geometry is also provided. For convenience, during the experiment, the mass center was moved below the bearing center $(+z)$ to make the platform stable by adjusting a vertical counterweight. The counterweight can later be moved up to make the platform neutrally stable for other experiments. In this case, the inertia can be adjusted using the parallel axis theorem [25].

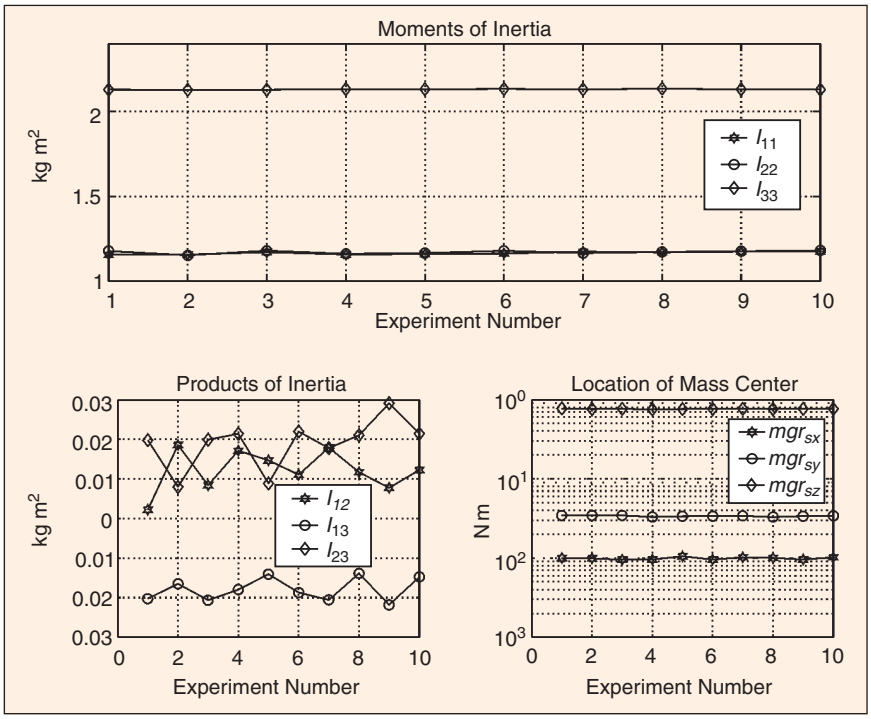

Figure 13. *Results of the inertia estimation for a series of ten experiments.*

The results of the estimation are shown in Table 1. Figure 13 shows graphically the results of the ten experiments. In Figure 13, $I_{11}, I_{12}, I_{13}, I_{22}, I_{23}$, and I_{33} are the elements of $\mathbf{I}$ in the spacecraft body frame $\mathcal{S}$.

The results of the experiments show remarkable consistency, especially for the principal moments of inertia I_{11}, I_{22}, and I_{33}. The products of inertia and the center of mass location have very small values. As a result, their estimation is more susceptible to numerical and measurement errors, noise, etc. The standard deviations are $\sigma(I_{11}) = 0.0075$, $\sigma(I_{22}) = 0.0091$, $\sigma(I_{33}) = 0.0022$, $\sigma(I_{12}) = 0.0049$, $\sigma(I_{13}) = 0.0028$, $\sigma(I_{23}) = 0.0060$, $\sigma(mgr_{sx}) = 0.0011$, $\sigma(mgr_{sy}) = 0.0019$, and $\sigma(mgr_{sz}) = 0.0160$. Note that because some components such as wires and counterweights were not modeled, the experimental values are somewhat larger than those found with the AutoCAD model.

Results from the Implementation of an LQR Controller

In this section, we present some experimental results for a simple stabilizing controller. Several assumptions are made to linearize the equations. First, the small product-of-inertia terms were neglected. Second, assuming small Eulerian angles ϕ and θ, one obtains that $\dot{\phi} \approx p$, $\dot{\theta} \approx q$ and $\dot{\psi} \approx r$, where p, q, and r are the angular velocity components of the platform expressed in a body-fixed frame. Third, assuming that p, q, and r are also small, the equations of motion (1) and (2) can be linearized about the origin. The resulting system can be written in the standard form

$$\dot{x} = Ax + Bu, \tag{4}$$

where $x = [\phi, p, \theta, q, \psi, r]^T$ and

$$A = \begin{bmatrix} 0 & 1 & 0 & 0 & 0 & 0 \\ 0 & 0 & 0 & 0 & 0 & 0 \\ 0 & 0 & 0 & 1 & 0 & 0 \\ 0 & 0 & 0 & 0 & 0 & 0 \\ 0 & 0 & 0 & 0 & 0 & 1 \\ 0 & 0 & 0 & 0 & 0 & 0 \end{bmatrix}, \quad B = \begin{bmatrix} 0 & 1 & 0 \\ -(1/I_{11}) & 1/(2I_{22}) & 0 \\ 0 & 0 & 0 \\ 0 & \sqrt{3}/(2I_{22}) & 0 \\ 0 & 0 & 0 \\ 0 & 0 & 1/I_{33} \end{bmatrix}. \tag{5}$$

The control input is $u = [M_1, M_2, M_3]^T$, where M_ℓ, $\ell = 1,2,3$ is the torque applied to the ℓth wheel. An LQR controller that minimizes a quadratic cost of the form

Table 1. Results of inertia and center of gravity estimation.

Identified Inertia Matrix			*mgr*	AutoCAD		
1.1667	0.0107	–0.0185	0.0101	1.027	0.000	0.000
0.0107	1.1671	0.0159	0.0323	0.000	1.034	0.000
–0.0185	0.0159	2.1291	0.7630	0.000	0.000	1.869

$$J = \int_0^\infty \left\{ x^T Q x + u^T R u \right\} \, dt, \tag{6}$$

where $Q \geq 0$ and $R > 0$, and stabilizes ϕ, θ, ψ, p, q, and r can be designed using standard methods [27]. Using $Q = \text{diag}[1,1,1,1,1,10]$ and $R = \text{diag}[1,1,1]$, the state-feedback control $u = Kx$ with

$$K = \begin{bmatrix} -0.9659 & -1.7769 & 0.2589 & 0.6674 & 0 & 0 \\ 0.2589 & 0.3107 & 0.9659 & 1.8727 & 0 & 0 \\ 0 & 0 & 0 & 0 & 1 & 3.7760 \end{bmatrix} \tag{7}$$

was obtained. Experimental results for two different initial conditions with this LQR controller are shown in Figure 14. Also shown, in Figure 15, are the results from the numerical simulations. The experimental and numerical results are close except for the ψ/r channel owing to torque saturation of the z-axis wheel, as is clearly evident from the bottom plots of Figure 14.

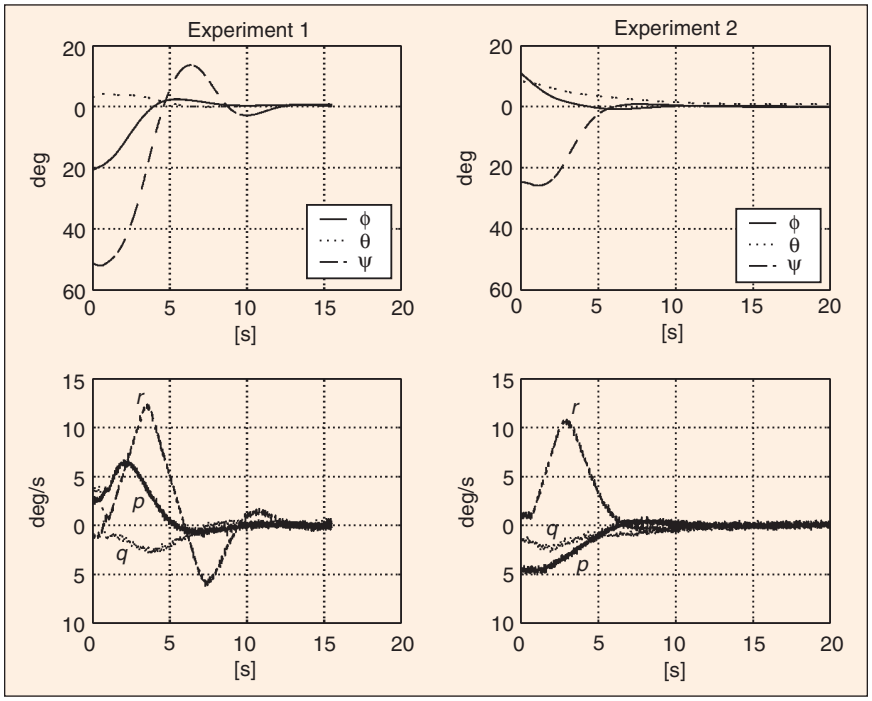

Figure 14. *Experimental results of the LQR controller.*

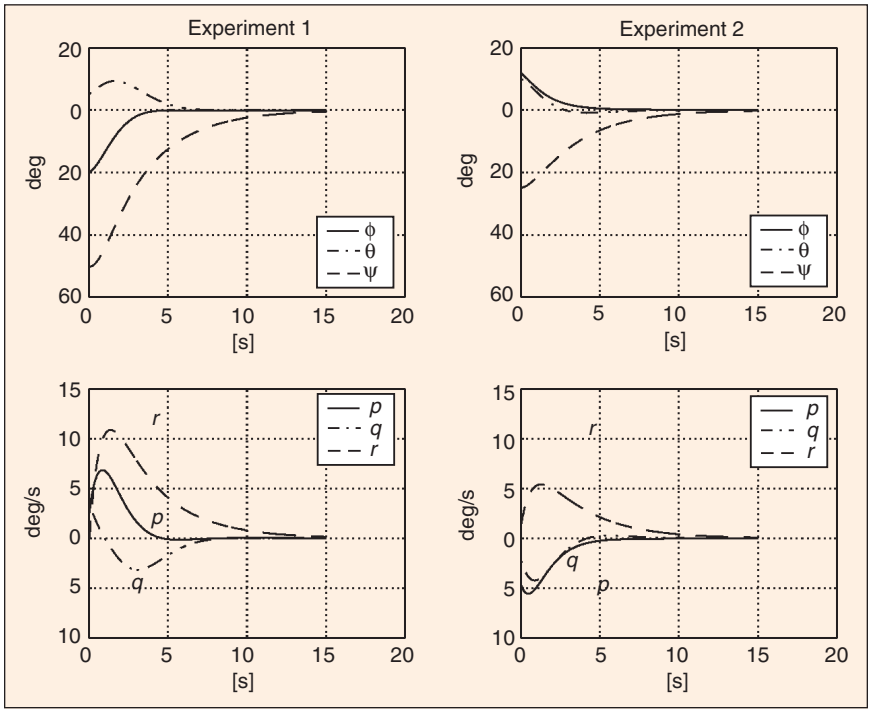

Figure 15. *Numerical simulation results with the LQR controller.*

Conclusions

A spacecraft simulator facility has been designed and constructed at the Georgia Institute of Technology School of Aerospace Engineering. The simulator is to be used primarily for educating undergraduate students in spacecraft attitude dynamics and control. During its construction, several technical issues were encountered, including choice of motors, sizing of the wheels, and sensor range and resolution. Identification of motor dynamics and friction, as well as motor damping estimation, was deemed necessary to better characterize the motor properties. A special-purpose software was written to implement the control laws and schedule the necessary hardware tasks. The mass and moments of inertia of the spacecraft simulator were estimated using a least-squares approach by commanding known torques and observing the angular acceleration response. The results from several experiments showed good consistency and corroborated the mass and inertia values obtained from an AutoCAD model. After careful balancing of the platform, an LQR controller was designed, based on a linearized model of the system, and successfully implemented on the simulator. The experimental results were consistent with those obtained from numerical simulations.

Acknowledgments

The work described in this article was supported in part by AFSOR Award

F49620-00-1-0374 and NSF Award CMS/REU-9996120. We also thank Dongwon Jung for the implementation of the recursive least-squares estimation algorithm.

References

[1] K. Lau, M. Colavita, G. Blackwood, L.R.M. Shao, and D. Gallagher, "The new millennium formation flying optical interferometer," in *Proc. AIAA GNC Conf.*, New Orleans, LA, paper AIAA 97-3820, 1997, pp. 650-656.
[2] R.L. Grogan and R.A. Laskin, "On multidisciplinary modeling of the space interferometry mission," in *Proc. American Control Conf.*, Philadelphia, PA, 1998, pp. 1558-1562.
[3] A. Robertson, T. Corazzini, and J. How, "Formation sensing and control technologies for a separated spacecraft interferometer," in *Proc. American Control Conf.*, Philadelphia, PA, 1998, pp. 1574-1579.
[4] P. Wang, F.Y. Hadaegh, and K. Lau, "Synchronized formation rotation and attitude control of multiple free-flying spacecraft," *J. Guidance, Contr., Dynam.*, vol. 22, no. 1, pp. 28-35, 1999.
[5] C. Sabol, R. Burns, and McLaughlin, "Satellite formation flyng design and evolution," *J. Spacecraft Rockets*, vol. 38, no. 2, pp. 270-278, 2001.
[6] R.W. Beard, J. Lawton, and F.Y. Hadaegh, "A feeback architecture for formation control," in *Proc. American Control Conf.*, Chicago, IL, 2000, pp. 4087-4091.
[7] M. de Queiroz, V. Kapila, and Q. Yan, "Adaptive nonlinear control of multiple spacecraft formation flying," *J. Guidance, Contr., Dynam.*, vol. 23, no. 3, pp. 385-390, 2000.
[8] D.J. Jezewski, J.P. Brazzel Jr., E.E. Prust, B.G. Brown, T.A. Mulder, and D.B. Wissinger, "A survey of rendezvous trajectory planning," in *Proc. AAS/AIAA Astrodynamics Conf.*, AAS paper 91-505, Durango, CO, 1991, pp. 1373-1396.
[9] T.A. Mulder, "Autonomous rendezvous trajectory planning," in *Proc. 2nd AAS/AIAA Spaceflight Mechanics Conf.*, AAS Paper 92-104, Colorado Springs, CO, 1992, pp. 709-719.
[10] M.R. Helton, "Refurbishable satellites for low-cost communications systems," *Space Commun. Broadcasting*, vol. 6, pp. 379-385, 1989.
[11] D. Manouchehri and A.J. Mauceri, "Automated resupply of consumables: Enhancement of space commercialization opportunities," in *Proc. 5th Annual Workshop Space Operations Applications and Research (SOAR 1991)*, vol. 1, 1991, pp. 407-411.
[12] A. Das, J.L. Berg, G.A. Norris, D.F. Cossey, T.J. Strange, and W.T. Schlaegel, "ASTREX—A unique test bed for CSI research," in *Proc. 29th IEEE Conf. Decision and Control*, Honolulu, HI, 1990, pp. 2018-2023.
[13] M.A. Brown and G. Creamer, "RESHAPE: A laboratory for research in satellite control and control/structures interaction," Naval Research Laboratory, Spacecraft Engineering Department, Washington, D.C., Tech. Rep. 1992.
[14] D. Bernstein, H. McClamroch, and A. Bloch, "Development of air spindle and triaxial air bearing testbeds for spacecraft dynamics and control experiments," in *Proc. American Control Conf.*, Arlington, VA, 2001, pp. 3967-3972.
[15] B.N. Agrawal and R.E. Rasmussen, "Air bearing based satellite attitude dynamics simulator for control software research and development," in *Proc. SPIE AeroSense, Modeling, Simulation, and Visualization Conf.*, Orlando, FL, 2001, pp. 204-214.
[16] W. Stadler, *Analytical Robotics and Mechatronics*. New York: McGraw-Hill, 1995.
[17] J.A. Mangus, C. Passerello, and C. VanKarsen, "Estimating rigid body properties from force reaction measurements," in *Proc. 11th Int. Modal Analysis Conf.*, Kissimmee, FL, 1993, pp. 469-472.
[18] M.A. Stebbins and D.L. Brown, "Rigid body inertia property estimation using a six-axis load cell," in *Proc. 16th Int. Modal Analysis Conf.*, Santa Barbara, CA, 1998, pp. 900-906.
[19] S. Tanygin and T. Williams, "Mass property estimation using coasting maneuver," *J. Guidance, Contr., Dynam.*, vol. 20, pp. 625-632, 1997.
[20] A.Y. Lee and J.A. Wertz, "In-flight estimation of the Cassini spacecraft inertia tensor," *J. Spacecraft*, vol. 39, no. 1, pp. 153-155, 2002.
[21] E.V. Bergmann, B.K. Walker, and D.R. Levy, "Mass property estimation for control of asymmetrical satellites," *J. Guidance, Contr. Dynam.*, vol. 10, pp. 483-491, 1987.
[22] R.F. Richfield, B.K. Walker, and E.V. Bergmann, "Input selection for a second order mass property estimator," *J. Guidance, Contr. Dynam.*, vol. 11, pp. 207-212, 1988.
[23] J. Ahmed, V.T. Coppola, and D. Bernstein, "Adaptive asymptotic tracking of spacecraft attitude motion with inertia matrix identification," *J. Guidance, Contr. Dynam.*, vol. 21, pp. 684-691, 1998.
[24] R.H. Bishop, S.J. Paynter, and J.W. Sunkel, "Adaptive control of space station with control moment gyros," *IEEE Contr. Syst. Mag.*, vol. 12, pp. 23-28, 1992.
[25] P.C. Hughes, *Spacecraft Attitude Dynamics*. New York: Wiley, 1986.
[26] K.J. Åström and B. Wittenmark, *Adaptive Control*, 2nd ed. Boston, MA: Addison Wesley, 1995.
[27] R.F. Stengel, *Optimal Control and Estimation*. New York: Dover, 1994.

ByungMoon Kim earned his B.S. in 1994 from Inha University, Korea, and his M.S. in 1999 from the Georgia Institute of Technology, both in aerospace engineering. Currently, he is a Ph.D. student in computer science at the Georgia Institute of Technology. His current research interests are computer graphics, modeling, computer vision, animation, simulation, dynamics, and control theory and experiments.

Efstathios Velenis received his engineering diploma in mechanical engineering at the National Technical University of Athens in March 1999. In December 2000 he received his M.Sc. from the School of Aerospace Engineering, where he is currently a Ph.D. candidate. His research includes the development of a spacecraft simulator facility, control of active magnetic bearings, and tire friction modeling and control for high-speed wheeled vehicles.

Patrick Kriengsiri is an undergraduate student in the School of Aerospace Engineering at the Georgia Institute of Technology.

Panagiotis Tsiotras received his Ph.D. in aeronautics and astronautics from Purdue University in 1993, his M.Sc. in aerospace engineering from Virginia Tech in 1987, and his engineering diploma in mechanical engineering from the National Technical University of Athens, Greece, in 1986. He also has an M.Sc. degree in mathematics from Purdue University (1992). From 1994-1998 he was an assistant professor with the Department of Mechanical and Aerospace Engineering at the University of Virginia. Since September 1998 he has been an associate professor in the School of Aerospace Engineering at the Georgia Institute of Technology and director of the Dynamics and Controls Systems Laboratory (DCSL). He is a recipient of the NSF Career Award (1996). He is an associate editor of the *AIAA Journal of Guidance, Control, and Dynamics*. His research interests include dynamics and control of nonlinear systems, optimal and robust control, and their applications to mechanical and aerospace systems. He can be contacted at the School of Aerospace Engineering, Georgia Institute of Technology, Atlanta, GA 30332-0150, U.S.A., p.tsiotras@ae.gatech.edu.